An open-closed flow separation in a compressor radial diffuser

Pierre Duquesne, Jerome Dombard, Nicolas Poujol, Alexis Giauque

An open-closed flow separation in a compressor radial diffuser

Pierre Duquesne
Associate Professor
Ecole Centrale de Lyon,
CNRS, Universite Claude Bernard Lyon 1,
INSA Lyon, LMFA, UMR5509,
69130, Ecully, France
Email: pierre.duquesne@ec-lyon.fr

Jerome Dombard
CERFACS
42 Avenue Gaspard Coriolis,
Toulouse, France

Nicolas Poujol
PhD student
Ecole Centrale de Lyon,
CNRS, Universite Claude Bernard Lyon 1,
INSA Lyon, LMFA, UMR5509,
69130, Ecully, France

Alexis Giauque
Associate Professor
Ecole Centrale de Lyon,
CNRS, Universite Claude Bernard Lyon 1,
INSA Lyon, LMFA, UMR5509,
69130, Ecully, France

Large-Eddy Simulations (LES) results are used to track flow separation zones in a splittered vaned radial diffuser near the compressor best efficiency at high rotation speed. The topology analysis reveals some closed separations at the corner of the blade and hub or shroud surface. In addition, an open-closed flow separation at the main blade pressure side is observed for the first time. The surface separation has the shape of a sheet at the blade mid-span and the associated separation line is delimited only at its downstream extremity by a trailing edge node. This flow separation process is robust to a small shift in operating condition and the separation surface remains essentially unchanged. A large flow rate variation converts the open-closed separation into a more classic closed separation. The evolution in time of the separation surface is also observed and the authors conclude to the unsteady existence of the open-closed separation.

Nomenclature

Latin

$\dot{m}$	=	Mass flow rate [kg/s]
C_x	=	Axial extent of the impeller
C_{pd}	=	Diffuser recovery coefficient
g	=	Surface genus
P	=	Pressure [Pa]
r	=	Specific gas constant [J/(kg·K)]
T	=	Temperature [K]

Greek Symbols

γ	=	Adiabatic coefficient
π	=	Pressure ratio
ΣN	=	Number of nodes and foci
ΣS	=	Number of saddle points

Subscripts

c	=	Compressor (impeller + radial diffuser)

ref = Reference (value)
s = static
std = Standard
t = total
0, 1, 2, 3 = Position refer to Figure 1
Superscripts
$t-s$ = total to static
Acronyms
LE = Leading Edge
LES = Large Eddy Simulation
TE = Trailing Edge

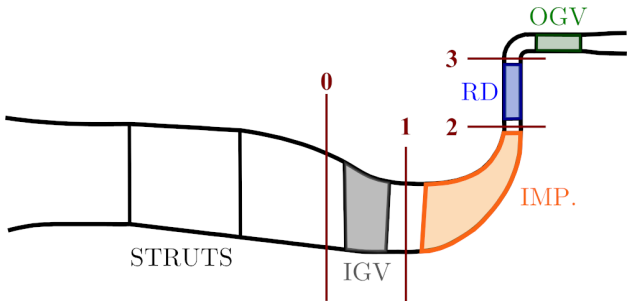

Fig. 1. Meridional view of the compressor

1 Introduction

The boundary layer flow separation can be described as the ejection of fluid from the boundary layer toward the flow away from the wall (according to Prandtl [1]). The flow separation is a generic problem in both fundamental fluid mechanics and industrial flows. Its emergence in turbomachinery induces numerous problems such as performance losses, unstable operation or noise generation. The flow separation in turbomachinery is generally three dimensional, unsteady, turbulent and confined. As shown in this work, the three-dimensional and confined aspects may lead to the emergence of an open-closed flow separation pattern in a splittered vaned radial diffuser. Open-closed separations are rarely observed. As presented in this article, the case in the radial diffuser deviates from the previously reported topology observed for a cylinder with a hemispherical [2]. The classification of open and closed separation is still a subject of discussion in the community since the observation of an open separation by Wang [3]. The flow separation surface, or the manifold, corresponds to the surface in the fluid domain where the flow is accumulated near the wall and ejected away from the wall. The separation surface does not correspond to the isosurface of zero velocity or the boundary of the backflow zone. In a steady approach, the flow separation surface is connected to a particular skin friction line at the wall: the separation line. The skin friction along a separation line is not necessarily zero. Points with zero skin friction are named critical points. A closed separation has a separation line passing through and bounded by critical points. The analysis of the organization of skin friction lines around zero-friction points and the separation line is commonly referred to as the topological analysis of flow separation. This type of analysis based on the work of Poincaré [4] on differential equations and applied to the fluid mechanics by Legendre have been abundantly used in the last sixty years, particularly in external flows, to analyze three-dimensional flow separation. This method of analysis is crucial because there is no local indicator for the occurrence of separation at a flow-specific location [5]. An analysis of the skin friction Jacobian matrix reveals that critical points can be associated with only three types of skin friction patterns, namely the node, focus, and saddle point. Nodes and foci can either attract if skin friction lines converge or repel otherwise. In addition, the proportion between nodes/foci in one part and saddle points in another part must respect a topology rule based on the surface genus. In opposition to closed separation, for an open separation, critical points can exist but the separation line does not pass through them according to Tobak et al. [6]. The two typical examples used to introduce open separation are a round-nosed body of revolution at high angles of attack [3] and delta wing [5]. More recently, Surana et al. [7] used hyperbolic approach on plane and surface diffeomorphic to a sphere to confirm analytically the existence of open separation. The only open separation topological organisation corresponds to a separation line with the shape of a concentric circle around the critical point (stable limit cycle). Surana et al. [7] also present the existence of a third category of flow separation: the open-closed separation. The open-closed separation has a separation line bounded only on one side by a critical point. These references set the context in which this study is carried out. This present work presents and analyses the occurrence of an open-closed separation. To the best of the author's knowledge, it is the first time that such structure is evidenced in a turbomachinery flow. Since the implications in terms of flow control and stability are significative, great care is taken to ensure the characterization of the separation.

Analysis is based on an time-averaged flow field extracted from Large-Eddy Simulation (LES). The numerical methodology is first presented. A topological analysis is then proposed to provide a clear map of the closed separation zones that also occur in the radial diffuser. Based on skin friction lines and 3D-streamlines the open-closed separation is located on the main blade pressure side. Mechanism, origins and robustness of this peculiar separation zone are proposed. The last section is dedicated to the persistence of the open-closed separation flow structure in an unsteady context.

2 Numerical and experimental setup

The test case is a research centrifugal compressor stage designed and manufactured by Safran Helicopter Engines. The compressor stage includes four blade rows: axial inlet guide vanes (IGV), a backswept splittered impeller (IMP), a splittered vaned radial diffuser (RD) and axial outlet guide vanes (OGV). A meridional scheme of the compressor is provided in Figure 1. The overall stage total to static pressure ratio is around 4. The Mach number based on the peripheral velocity at the exit radius of the impeller is around 1.2.

In the framework of the European project FLORA

(FLOw control in RAdial compressor), the compressor flow field is investigated with experimental and numerical methods [9]. The purpose of the project is to investigate aerodynamic phenomena limiting the compressor operating range and to test control methods aimed at extending this range. In this context, suction holes are present at the hub and shroud near the main blade suction side of the diffuser. It is important to note that the diffuser is designed to operate without flow control at the nominal operating point. The suction holes from the same interblade channel are interconnected and linked to the atmosphere through a controlled valve. However, for the purposes of this paper, the control is not utilized, and the valve remains completely closed.

The simulation domain is composed of 1/3 of the full machine [10]. The technological effects of the experimental compressor stage are included in the simulation domain, i.e. endwall fillets, cavities of suction at the hub and shroud of the radial diffuser. Non-reflective boundary conditions [11] are set at the inlet of the domain where one-dimensional values of total pressure and total temperature are imposed without inlet turbulence. Since the full intake is meshed and the characteristic size and turbulence intensity are small at its inlet, imposing a laminar inlet is expected to be a good trade off and have few influence on the overall physics. Periodic conditions are applied on the azimuthal boundaries and walls are considered adiabatic. The simulation is performed using the massively parallel unstructured code AVBP [12] that solves the compressible Navier-Stokes equations. The convective operator is discretized by the Lax-Wendroff scheme [13] (2^{nd} order accurate) and an explicit time advancement. The time step based on the smallest cell in the simulation domain and a CFL number of 0.9 provides a time step equals to $\Delta t = 1.9.10^{-8} s$. The time step is roughly 10^5 smaller than a characteristic convective time.

The Sigma Sub-Grid Scale model (SGS) is used [14]. Two instances of AVBP (one for the static domain and the other for the rotating one) are coupled at interfaces between static and rotating domains using a Single Program-Multiple Data (SPMD) paradigm [15]. In each domain, an instance solves the filtered Navier-Stokes equations and an exchange of primitive variables is performed by mean of a 3^{rd} order interpolation at the interface under a synchronous process using overset grids [16].

The unstructured meshing approach uses tetrahedra that fill the simulation domain. This mesh is composed of 45 million elements for the inlet plenum and IGV, 209 million elements for the impeller and 69 million elements for the radial and axial diffuser leading to a total size of around 323 million elements. In addition, cavities at the hub and shroud of the radial diffuser, for flow control purpose, have been meshed but no suction is performed in these cavities. To simplify the post-processing process while also reducing its cost, the original 323 millions cells unsteady and average solution are the interpolated onto a structured mesh comprising 25 millions cells.The simulation has been performed over 2800 CPU cores from the Cobalt CCRT calculator at a constant rotation speed and changing continuously in time the outlet back pressure, following the methodology of Dombard et al. [17]. Seven operating points have been simulated and each time-averaged solution has been acquired during approximately ten impeller revolutions. More details are provided in Table 1. The characteristic surface sizes are provided in Table 2 for the different components. These mesh sizes have been set to target a mean y+ around one hundred that has been checked a posteriori and a wall function is applied. This strategy has been used to capture unsteady structures resolved by LES while keeping a tractable mesh and affordable computational cost, still yielding satisfactory results according to Dombard et al.

Figure 2 presents the operating points simulated at high rotation speed. The compressor total-to-static pressure ratio (π_C^{t-s}), the diffuser recovery coefficient (C_{pd}) and the standard mass flow rate ($\dot{m}_{std}$) are respectively defined by:

$$\pi_c^{t-s} = \frac{P_{s,3}}{P_{t,0}} \tag{1}$$

$$C_{pd} = \frac{P_{s,3} - P_{s,2}}{P_{t,2} - P_{s,2}} \tag{2}$$

$$\dot{m}_{std} = \dot{m} \frac{P_{ref}}{P_{t,0}} \sqrt{\frac{r\gamma_{ref} T_{t,0}}{r_{ref}\gamma T_{ref}}} \tag{3}$$

Values are normalised by reference values for confidentiality purpose. Only one high iso-speed is simulated and mostly one operating point is considered for the analysis, operating point A (denoted OPA, see Figure 2). This operating point is near the best efficiency point, induces a high-pressure ratio and an effective static pressure recovery from the diffuser. The nearest operating points at lower and higher flow rate are only considered as perturbation of the operating condition to appreciate the robustness of the flow separation. Operating points B and C are used to present the evolution of the flow separation lines with a large change in the flow rate.

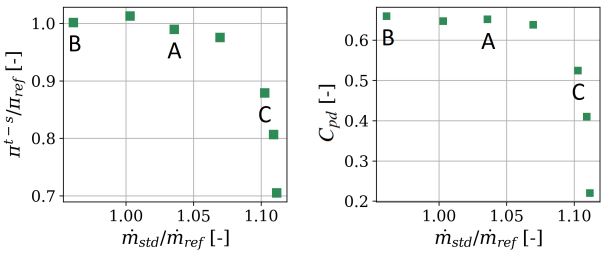

Fig. 2. LES compressor performance map and diffuser recovery coefficient

In OPA the flow is similar in each main channel of the diffuser (between two main blades) of the diffuser, consequently the analysis domain is restricted to one channel. The

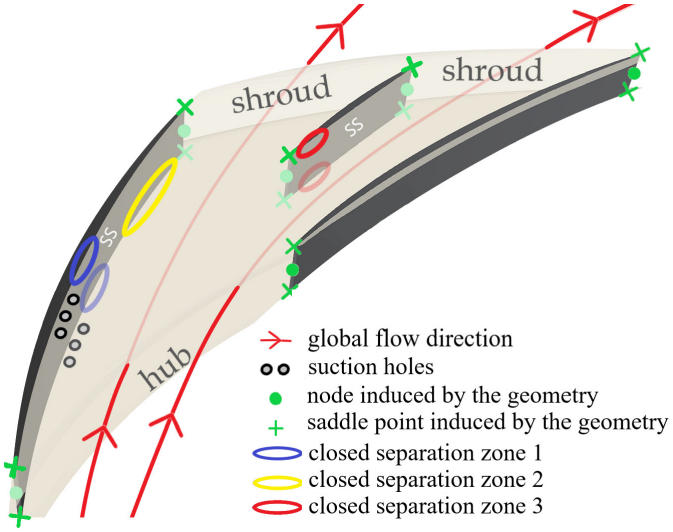

Fig. 3. Domain of analysis in the radial diffuser

analysis domain is delimited by the main blade suction side, the adjacent main blade pressure side and the shroud and hub surfaces. The domain includes also a splitter blade as shown in Figure 3. The global flow direction and the suction holes locations are presented in Figure 3. The skin friction lines are approximated by the 2D streamlines using the velocity field at the first cell from the walls.

3 Separation analysis on the averaged flow field

3.1 Closed separation zones

In this section, a quick overview of the different closed separation zones is presented. In closed separation, the separation line starts and ends at critical points. An analysis of skin friction lines has been conducted to locate all critical points. The three-dimensional streamlines have been observed to identify the different separation zones. Since this study has been already presented in [18], only the main steps are recalled hereafter. The geometry of the analysis domain has a genus (g) of two and the topology rule becomes :

$$\Sigma N - \Sigma S = 2 - 2g = -2 \tag{4}$$

With ΣN the number of nodes and foci and ΣS the number of saddle points. The list of critical points is provided in Table 3. The amount of nodes, foci and saddle points respect the topology rule is given in Eq. 4.

The analysis domain proposed is not the complete system but only a portion of the radial diffuser. To respect the topology rule in this case, some critical points need to be added for the boundary condition (refer to Surface Partition and Splitting Critical Points or SCP in Table 3 or in [18]).

The geometry category in Table 3 (represented in green in Figure 3) corresponds to the flow passing solid volumes. For the splitter blade, a node (the stagnation point) emits friction lines at the leading edge and another node collects the skin friction lines at the trailing edge. Four saddle points complete the flow passing solid volumes at the leading and trailing edges for the junction between the splitter and the hub and the shroud. For the main blades, same geometric critical points as for the splitter blade are present. With the chosen domain of analysis, main blade critical points are counted the half. For the pressure side of the first main blade, two half-nodes and four half-saddle-points are present. The count is the same for the suction side of the second main blade. At that stage the number of critical points respect the topology rule without any closed flow separation.

Other critical points correspond to closed separation zones. Flow is ejected from the boundary layer and a separation line connects the different critical points. One separation zone is isolated from the others: the separation line from one zone does not connect with critical points of another zones. The first zone (denoted 1 in Table 3 and colored in blue in Figure 3) corresponds to a small corner separation at the hub surface and the main blade suction side. The associated critical points are two saddle points and two foci. The same separation structure (denoted 1' in Table 3) is present at the corner with the shroud surface. Downstream of the first separation zone, the boundary layer is weakened and the adverse pressure gradient induces a second corner separation (in yellow in Figure 3) at the hub surface. This zone includes three saddle points and three foci. The flow deviation at the endwalls along the diffuser induces a high incidence on the splitter leading edge. This leads to a separation zone at both the corner splitter blade suction side and that of the hub or shroud (denoted 3 and 3' in Table 3 and colored red in Figure 3). Both zones 3 and 3' are composed by two saddle points and two foci. As presented in Table 3, the topology rule given in Eq. 4 is respected when taking into account zones 1, 1', 2, 3 and 3'.

3.2 Open-closed separation

As depicted in Figure 4, another separation surface seems to exist at the main blade pressure side. The streamlines from the hub (in yellow in Figure 4) and from the shroud (in green in Figure 4) converge at mid-span. This induces a flow ejection from the main blade pressure side wall to the channel far from the wall. The separation surface corresponds to a sheet of ejection where streamlines converge from the hub and from the shroud surfaces.

The separation surface is linked to a particular skin friction line at the main blade pressure side surface: a separation line. This separation line is represented by the red line in Figure 5, and corresponds to the line where friction lines converge. The separation line finishes (downstream end) at the trailing edge node induced by the main blade geometry. However, this node exists even if the separation does not occur. The separation line starts (upstream end of the separation line) at an ordinary location (not a critical point) of the skin friction field. No zero, or reversed, friction vector is detected on the main blade pressure side surface. Trying to extend the separation line to the upstream node at the leading edge can be a tempting solution to "close" the separation.

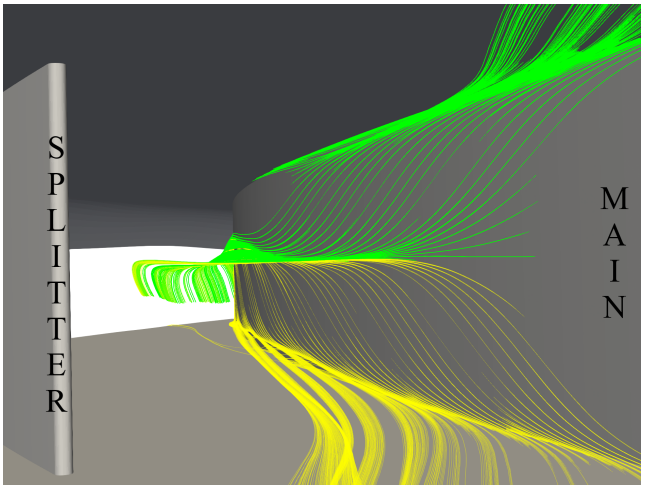

Fig. 4. Upstream view of the open-closed flow separation on the main blade inside the diffuser. Streamlines from the hub (from the shroud) are coloured in yellow (green)

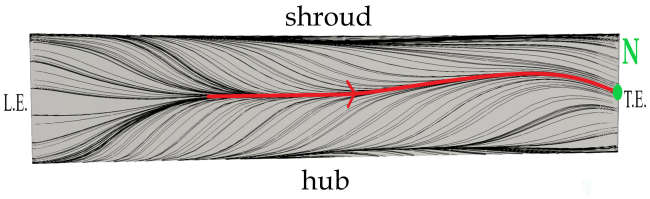

Fig. 5. Skin friction lines on the main blade pressure side. The separation line is colored in red. The leading edge (L.E.), the trailing edge (T.E.) and the blade exit node (N) are denoted.

But this solution does not appear correct as the flow separation surface does not extend up to the leading edge:

- Streamlines of the separation surface do not come from the leading-edge nodal stagnation point.
- Streamlines emitted at the wall near the leading edge at pressure side remain at the wall.

Using the previously presented terminology, this corresponds to an open-closed separation because only one end of the separation line is a critical point. In the hyperbolic approach used by Surana et al. [7], the open-closed separation can only occur in the case of a separation line originating from a saddle point and spiralling into a stable limit cycle. The present case is a separation line originating from the collision of streamlines without any node. But as noticed by Surana et al., their approach excludes toroidal surfaces which is precisely the present case.

As introduced previously, at the hub and shroud walls the skin friction lines deviate from the main blade suction side toward the pressure side. The skin friction pattern at the hub is visible in Figure 6. When skin friction lines at the hub (or shroud) surface reach the main blade pressure side, they continue onto the blade surface in the direction of the shroud (or the hub). The skin friction lines from the hub and from the shroud collide along the separation line on the main blade surface approximately at mid-span.

The collision mechanism at mid-span is peculiar and needs some specific conditions to occur. The first condition hints at a surface homeomorphic to a torus (i.e. the surface can be obtained from a torus and a set of continuous stretching and bending). This type of surface is excluded in the analysis made by Surana et al. In a toroidal surface the flow is confined inside the surface, the fluid particles can loop inside a torus without exiting the surface. In addition to the previous condition, the ”aspect ratio” of the toroidal geometry is important to ensure the collision of the skin friction lines (corresponding to the strong hyperbolicity conditions). For example, here the blade's aspect ratio is small (the ratio of the blade height to their chord length), if the blade's height is increased, the global flow tends to straighten the skin friction lines on the blade's surface, and the collision of skin friction lines disappears, as can be observed for example in a compressor cascade [8]. Finally, a condition on the flow field is the deviation of the flow near the wall in the same direction (i.e. here from the suction to the pressure side) at the hub and shroud surfaces.

In the present case, the deviation of the skin friction lines seems to be related to three effects: the passage vortex, the boundary layer suction system and the first closed separation zone (colored blue in Figure 3). In the boundary layer, the blade-to-blade curvature induces a secondary flow near the endwalls: the passage vortex. In the present case, the passage vortex at the hub and shroud surfaces deviates the flow both from the suction side to the pressure side. The boundary layer suction system is composed of several holes in the hub and shroud surfaces near the main blade suction side (see Figure 3). Every holes in the hub, and respectively in the shroud, are connected together to a collector. The suction system is not activated during the simulation. However, the pressure difference between the upstream and downstream suction system holes induces a flow inside the collector, as illustrated in Figure 7. The cut-plane is shown in Figure 6. As depicted, the flow exhibits high velocity in the diffuser (in red) compared to low velocity (in blue) in the suction system. As indicated by the streamlines, a flux is induced by the flow field from the diffuser into the aspiration system. This perturbation of the flow at the hub and shroud surfaces, induced by the boundary layer suction system, may have a potential blockage effect on the main flow near the endwalls. The closed flow separation zone 1 is just downstream the suction system (in blue in Figure 3 and 6). It is induced by the adverse pressure gradient at the suction side and probably also by the flow perturbation induced by the suction system. These three effects deviate the friction lines from the suction side to the pressure side at the hub and shroud surfaces.

3.3 Open-closed separation evolution with operating conditions

The open-closed separation robustness (i.e. the separation surface persistency under small perturbations) is adressed in this section. This aspect is investigated through the evolution of the separation line with the mass flow rate. For the nearest operating points at lower and higher mass

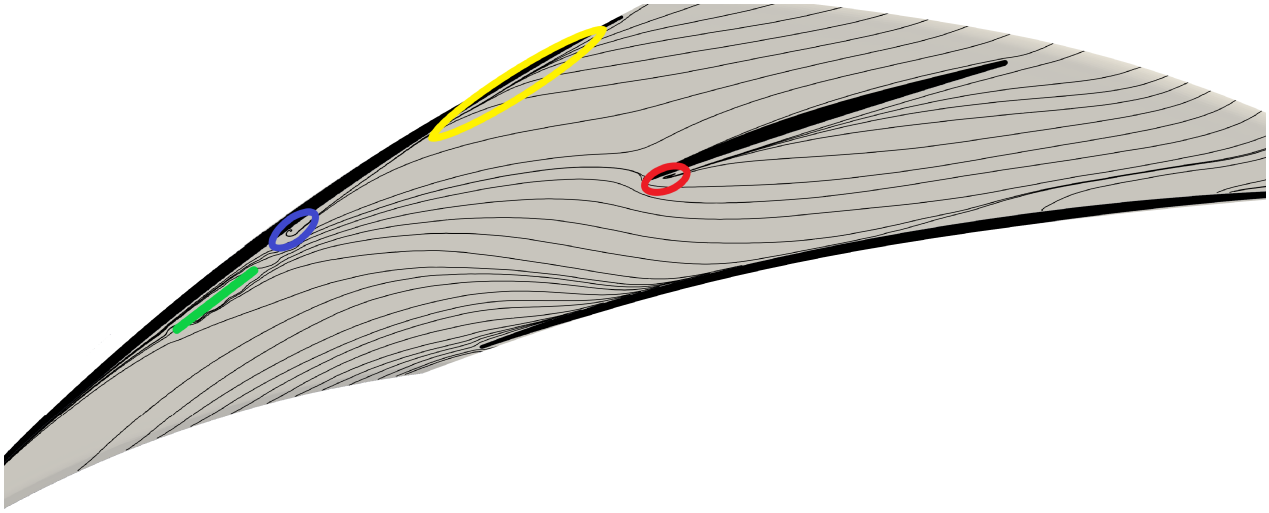

Fig. 6. Skin friction pattern at the hub. Separation zones are encircled using same color than as Figure 3, the green line represents the approximate position of the suction holes.

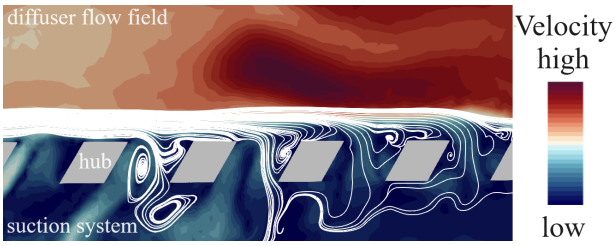

Fig. 7. Unsteady velocity field from low (blue) to high (red) velocity. White lines represent some streamlines. The 2D planar cut corresponds to the green line in Figure 6.

flow rates from OPA, the separation line does not change. The separation surface keeps the same shape and size. The open-closed separation is therefore robust in a range of $\pm 3\%$ of the mass flow rate. For operating points with a more significant flow rate variation (7% lower and 6% larger), the open-closed separation becomes a closed separation.

For the lower mass flow rate at OPB (see Figure 2), an alternate flow pattern arises (see previous work for further details [10]). In one channel over two, the separation line on the main blade pressure side keeps the open-closed organization. The separation surface still has an ejection sheet shape but with a reduced size. In the adjacent channel, as shown in Figure 8, the separation line at the main blade pressure side originates from a saddle point located at the blade-hub corner near the leading edge. Downstream, the separation line ends at a large focus on the last third of the chord. The flow separation is therefore closed one blade over two. The mechanism for the closed separation and blade-to-blade variations is explained in [19]. For OPC, the flow is similar in each channel. The separation line on the main blade originates from a saddle point on the pressure side and ends at a node in the last third of the blade surface (see Figure 8). The flow separation therefore is closed. For each case of closed separation on the main blade pressure side (OPB and OPC), the separation surface connects the blade surface and the hub surface instead of the ejection sheet in open-closed separation.

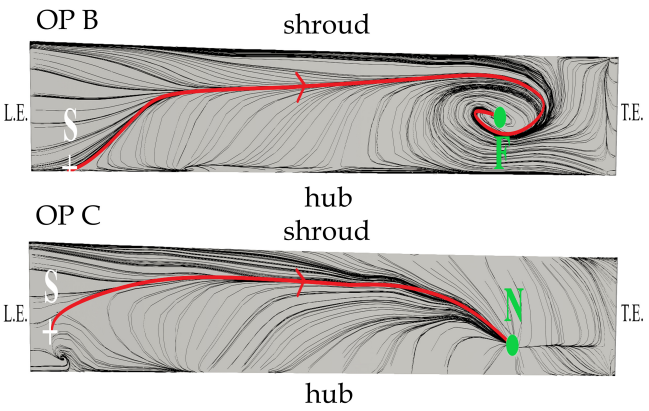

Fig. 8. Closed flow separation at mass flow rates OPB (top) and OPC (bottom)

4 Open-closed flow separation time evolution

The previous sections presented a flow separation mechanism based on an averaged flow field. The unsteady aspects of the flow in the diffuser can raise questions about the previous mechanism: Is the open-closed separation merely an artifact of the averaging process without realism in an instantaneous observation? To answer this question, instantaneous fields at OPA are investigated in this section. The unsteady data is composed of 38 snapshots, uniformly separated by 0,075 rotor rotations during a total of 2.85 rotor rotations. In a first approach, streamlines are generated for all unsteady fields (at the same position as in Figure 4). Three of them, spaced 0,9 rotor rotations apart, are represented in Figure 9. For all unsteady fields, the streamlines reveal a sheet of fluid ejection at the blade mid-span, as for the averaged field. The

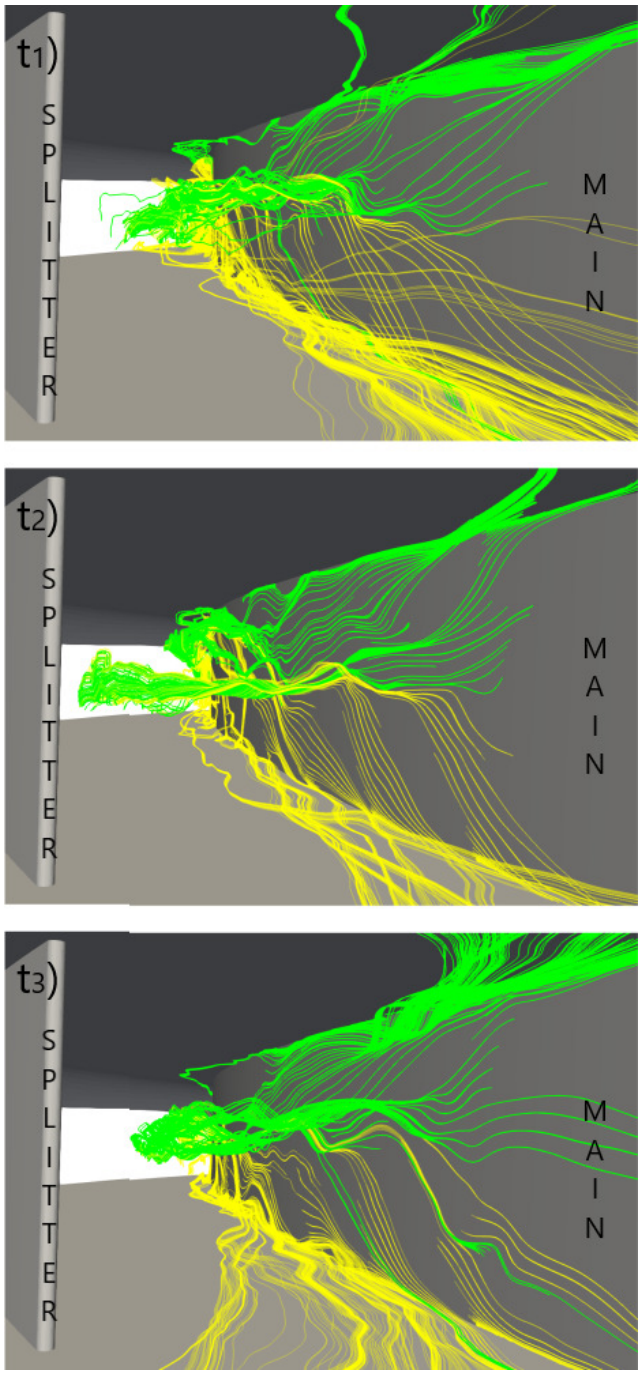

Fig. 9. Upstream view from of instantaneous streamlines at three instants. Streamlines from the hub (from the shroud) are coloured in yellow (green).

unsteady sheet of fluid is more disturbed than the one obtained with the average field. It can be explained by the unsteady flow at the diffuser inlet induced by the rotor and by the interaction of non-coherent turbulent structures with the flow separation manifold.

The skin friction lines from the unsteady flow field on the main blade are also determined using the same process as in Figure 5. Three skin friction patterns, corresponding to the same instants as for Figure 9, are presented Figure 10. The unsteady skin friction lines on the main blade pressure

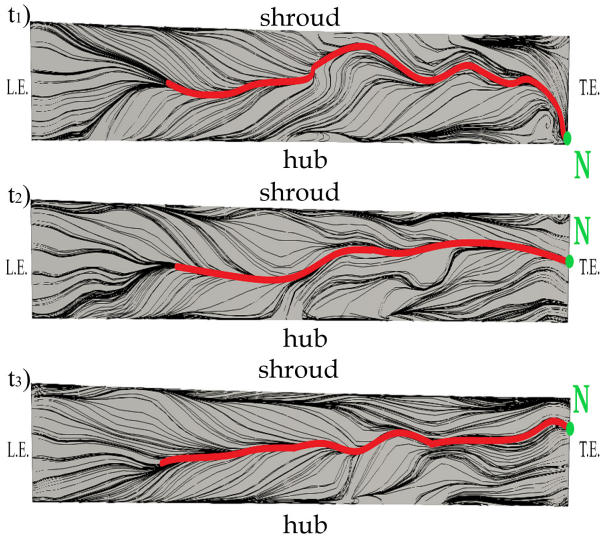

Fig. 10. Instantaneous Skin friction lines on the main blade pressure side. The separation line is colored in red. The leading edge (L.E.), the trailing edge (T.E.) and the node (N) are denoted.

side have the same structure as for the average skin friction lines. The separation line starts at an ordinary location (not a critical point), and finishes at a node located at the trailing edge. But a different separation line exists at each instant. These unsteady separation lines fluctuate around the average separation line position. The friction lines convergence towards the unsteady separation line is less regular, resulting in a more disturbed separation line than the average one. The closing node only moves on the trailing edge along the spanwise direction.

The previous approach tends to confirm that the open-closed separation is not an artefact of the averaging process. This first unsteady approach mimics the previous average analysis and cannot be trusted to follow the flow separation manifold. Unsteady streamlines, and unsteady skin friction lines, are by definition only parallel lines to the unsteady velocity field or skin friction fields. These should not be confused with the flow trajectory which defines the manifold in the unsteady analysis. In addition, the instantaneous link between the separation surface and the separation line at the wall in a turbulent and unsteady flow is not guaranteed [20]. To overcome these difficulties, the analysis is extended using a Lagrangian point of view. 41 particles are injected at the first third of the main blade chord along a line covering the channel height. Particles are injected near the wall but out of the boundary layer. At each extraction time step, the new position of existing particles is calculated and a new set of particles is injected. Main results are illustrated for a given time step in Figure 11. The figure has three sub-figures. The top subfigure is a 3D view with a similar perspective as Figure 4. The middle subfigure is a top view of the radial diffuser interblade channel, centered on one main blade. The bottom subfigure is a side view of the main blade pressure side. Each particle is represented by a circle colored by their initial position, in green for particles starting at the blade upper half

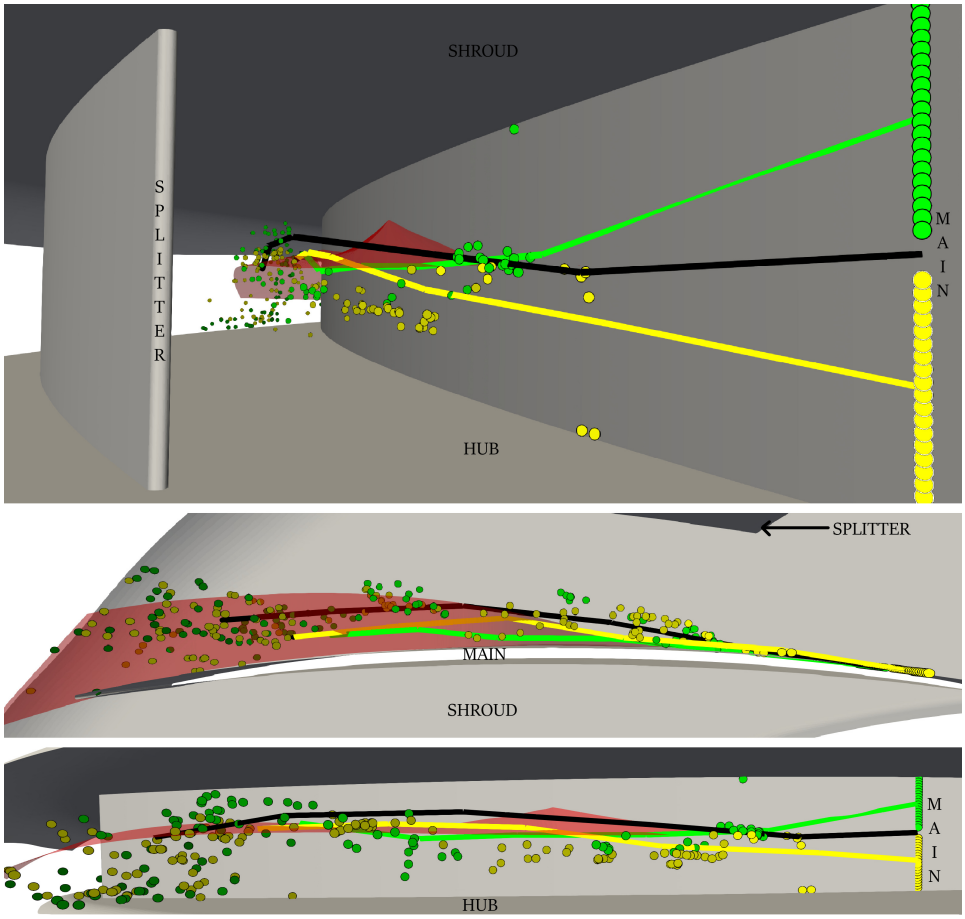

Fig. 11. From top to bottom: 3D view, top view and side view of Lagrangian Particles after 20 time steps. Particles colored in green (yellow) start at the blade upper (lower) half span. Particle color becomes darker when particles get older. Three trajectories colored by the initial position and in black at mid-span. Red transparent surface corresponding to the average manifold.

span (near the shroud) or in yellow for particles starting at the blade lower half span (near the hub). The particle color becomes darker when particles get older. Particles at their injection positions can be observed at the right of the figures. Oldest particles in the figure have been carried for ten time steps. Three trajectories are also represented and colored by the initial position and in black at mid-span. All trajectories are starting at the same time step and five time steps are represented. The red transparent surface corresponds to the average manifold reconstructed with the same streamlines as in Figure 4.

A majority of particles from the blade upper half and from the blade lower half starts to converge to the mid-span during the first time steps. Particles are blended and concentrated before the average flow separation manifold. When particles arrive at the proximity of the average flow separation manifold, they are pushed to the center of the interblade channel. Particles stop following the main blade surface and are ejected from the boundary layer. Thus, the unsteady Lagrangian approach tends to confirm the flow separation existence. When particles travel inside the average separation manifold zone, they are more and more dispersed in the flow field. Finally, particles tend to go to the hub surface to follow the diffuser exit bend. This description is representative of all observed time steps. The three selected trajectories seem to present a good agreement with the average separation manifold. Given the turbulent and unsteady nature of the flow, the particle-to-particle variability of the observed trajectories is not surprising.

In conclusion, the existence of an open-closed flow separation is confirmed by the unsteady analysis.

5 Conclusions

In this article, the different flow separation zones in a splittered vaned radial diffuser are presented based on LES results. Most of them are classical closed separations (with a separation line passing through and bounded by critical points). For the first time, an open-closed flow separation at the main blade pressure side is also observed. The average and unsteady flow separation surfaces (or manifold) correspond to the shape of a sheet at the blade mid-span. The separation line at the wall is composed of the convergence of friction lines to an ordinary point (not a critical point) and terminate at a node (a critical point), corresponding to an open-closed separation. This mechanism differs from the existing theoretical description, due to the confined aspect of the flow field. The open-closed separation zone is resilient to

a small variation of flow conditions. In case of an important variation of the flow rate, new critical points appear and the flow separation zone becomes a common closed separation. In the continuity of this paper, a work of generalization needs to be done. The main objective is to develop quantitative criteria for open-closed separation occurrence. For this, other examples need to be found in the confined flow community (including but not only in turbomachinery) and the hyperbolic approach needs to be adapted to toroidal surfaces.

Acknowledgements

This project has received funding from the Clean Sky 2 Joint Undertaking under the European Union's Horizon 2020 research and innovation program under grant agreement No. 820099. This publication reflects only the author's view and the JU is not responsible for any use that may be made of the information it contains. The authors would like to thank also Safran Helicopter Engines which supported this study.

References

[1] Prandtl, L., 1904. Über Flüssigkeitsbewegung bei sehr kleiner Reibung. *Heidelberg: Teubner (Leipzig).*!

[2] Hsieh, T., Wang, K. C., 1996. Three-dimensional separated flow structure over a cylinder with a hemispherical cap. *Journal of Fluid Mechanics*, 324.

[3] Wang, K. C., 1972. Separation Patterns of Boundary Layer over an Inclined Body of Revolution. *AIAA Journal*, 10 (8).

[4] Poincaré, H., 1916, Oeuvres de Henri Poincaré. *Académie des sciences, Ministère de l'éducation nationale.*

[5] Délery, J., 2001. Robert Legendre and Henri Werlé: Toward the Elucidation of Three-Dimensional Separation. *Annual Review of Fluid Mechanics*, 33 (1).

[6] Tobak, M., Peake, D. J., 1982. Topology of Three-Dimensional Separated Flows. *Annual Review of Fluid Mechanics*, 14 (1).

[7] Surana, A., Grunberg, O., Haller, G., 2006. Exact Theory of Three-Dimensional Flow Separation. Part 1. Steady Separation. *Journal of Fluid Mechanics*, 564.

[8] Gao, F., Ma, W., Zambonini, G., Boudet J., Ottavy, X.,Lu, L., Shao, L., 2015. Large-eddy simulation of 3-D corner separation in a linear compressor cascade.*Physics of Fluids*, 27.

[9] Poujol, N., Trébinjac, I., Duquesne, P., 2021. Effects of Inlet Guide Vanes on the Performance and Stability of an Aeronautical Centrifugal Compressor. *Journal of Turbomachinery*, 143.

[10] Moënne-Loccoz, V., Trébinjac, I., Poujol, N., Duquesne, P., 2020. Detection and analysis of an alternate flow pattern in a radial vaned diffuser. *Int. J. Turbomach. Propuls. Power*, 5 (1).

[11] Poinsot, T. J., Lelef, S. K., 1992. Boundary Conditions for Direct Simulations of Compressible Viscous Flows. *Journal of Computational Physics*, 101 (1).

[12] Schönfeld, T., Rudgyard, M., 1999. Steady and Unsteady Flow Simulations Using the Hybrid Flow Solver AVBP. *AIAA Journal,* , 37 (11).

[13] Lax, P. D., 1957. Hyperbolic Systems of Conservation Laws II. *Communications on Pure and Applied Mathematics*, 10 (4).

[14] Nicoud, F., Baya Toda, H., Cabrit, O., Bose, S., Lee, J., 2011. Using singular values to build a subgrid-scale model for large eddy simulation. *Physics of Fluids*, 23 (8).

[15] Wang, G., Papadogiannis, D., Duchaine, F., Gourdain, N., Gicquel, L., 2013. Towards Massively Parallel Large Eddy Simulation of Turbine Stages. In ASME Turbo Expo 2013: Turbomachinery Technical Conference and Exposition, American Society of Mechanical Engineers.

[16] Wang, G., Duchaine, F., Papadogiannis, D., Duran, I., Moreau, S., Gicquel, L., 2014. An overset grid method for large eddy simulation of turbomachinery stages. *Journal of Computational Physics*, 274.

[17] Dombard, J., Duchaine, F., Gicquel, L., Staffelbach, G., Buffaz, N., Trébinjac, I., 2018. Large Eddy Simulations in a Transonic Centrifugal Compressor. In ASME Turbo Expo 2018: Turbomachinery Technical Conference and Exposition, American Society of Mechanical Engineers.

[18] Duquesne, P., Chanéac, J., Mondin, G.,Dombard, J., 2022.Topology Rule-Based Methodology for Flow Separation Analysis in Turbomachinery. *Int. J. Turbomach. Propuls. Power*, 7 (3).

[19] Fiquet, A.L., Dombard, J. Poujol, N., Duquesne, P., 2023. Numerical investigation of a transonic centrifugal compressor at high rotational speed. In 15th European Turbomachinery Conference, European Turbomachinery Society.

[20] Sears, W. R., Telionis, D. P., 1975. Boundary-Layer Separation in Unsteady Flow. *SIAM Journal on Applied Mathematics*, 28 (1).

Table 1. Computational cost

Calculator	Cobalt 2800 cores
Physical time / revolution	11 hours
Physical time / operating point	5 days
CPU hours / operating point	310 thousand hours
CPU hours / characteristic curve	4 million hours

Table 2. Mesh sizes (Cx is the axial extent of the impeller)

Component	Surface mesh size/Cx
Inlet plenum	1.2×10^{-3}
Impeller	1.5×10^{-3}
Axial/radial diffuser	1.5×10^{-4}

Table 3. Critical point list

Origin	Node	Focus	Saddle
SCP	4	0	2
Geometry	4	0	8
Flow separation zone 1	0	2	2
Flow separation zone 1’	0	2	2
Flow separation zone 2	0	3	3
Flow separation zone 3	0	2	2
Flow separation zone 3’	0	2	2
Total	19		21